




# Original Research

## Cone photoreceptor reflectance variation in the northern tree shrew and thirteen-lined ground squirrel

Mina Gaffney<sup>1</sup> , Robert F Cooper<sup>1,2</sup>, Jenna A Cava<sup>1</sup> , Hannah M Follett<sup>1</sup>, Alexander E Salmon<sup>3,4</sup>, Susan Freling<sup>5</sup>, Ching T Yu<sup>3</sup>, Dana K Merriman<sup>6</sup>  and Joseph Carroll<sup>1,2,3</sup>

<sup>1</sup>Department of Ophthalmology & Visual Sciences, Medical College of Wisconsin, Milwaukee, WI 53226, USA; <sup>2</sup>Department of Biomedical Engineering, Marquette University, Milwaukee, WI 53233, USA; <sup>3</sup>Department of Cell Biology, Neurobiology, & Anatomy, Medical College of Wisconsin, Milwaukee, WI 53226, USA; <sup>4</sup>Translational Imaging Innovations, Inc., Hickory, NC 28601, USA; <sup>5</sup>Max Planck Florida Institute for Neuroscience, Jupiter, FL 33458, USA; <sup>6</sup>Department of Biology, University of Wisconsin Oshkosh, Oshkosh, WI 54901, USA  
Corresponding author: Joseph Carroll. Email: jcarroll@mcw.edu

### Impact statement

Cone photoreceptor reflectance is being explored as a possible biomarker of the overall health and function of the cell. Central to realizing this potential is advancing our understanding of the cellular origins of light capture and propagation within the photoreceptors. Our work provides important data to support the use of two cone-dominant animal models to further explore mechanisms of cone reflectance. Additionally, the observation of similar reflectance behavior to that of human cones (despite anatomical differences) can be used to inform theoretical models of the morphological origins of photoreceptor reflectance signals. Our data provide valuable baseline information against which to compare data from future studies in which cone structure or function is manipulated experimentally.

### Abstract

*In vivo* images of human cone photoreceptors have been shown to vary in their reflectance both spatially and temporally. While it is generally accepted that the unique anatomy and physiology of the photoreceptors themselves drives this behavior, the exact mechanisms have not been fully elucidated as most studies on these phenomena have been limited to the human retina. Unlike humans, animal models offer the ability to experimentally manipulate the retina and perform direct *in vivo* and *ex vivo* comparisons. The thirteen-lined ground squirrel and northern tree shrew are two emerging animal models being used in vision research. Both models feature cone-dominant retinas, overcoming a key limitation of traditional rodent models. Additionally, each possesses unique but well-documented anatomical differences in cone structure compared to human cones, which can be leveraged to further constrain theoretical models of light propagation within photoreceptors. Here we sought to characterize the spatial and temporal reflectance behavior of cones in these species. Adaptive optics scanning light ophthalmoscopy (AOSLO) was used to non-invasively image the photoreceptors of both species at 5 to 10 min intervals over

the span of 18 to 25 min. The reflectance of individual cone photoreceptors was measured over time, and images at individual time points were used to assess the variability of cone reflectance across the cone mosaic. Variability in spatial and temporal photoreceptor reflectance was observed in both species, with similar behavior to that seen in human AOSLO images. Despite the unique cone structure in these animals, these data suggest a common origin of photoreceptor reflectance behavior across species. Such data may help constrain models of the cellular origins of photoreceptor reflectance signals. These animal models provide an experimental platform to further explore the morphological origins of light capture and propagation.

**Keywords:** Adaptive optics scanning light ophthalmoscopy, AOSLO, photoreceptors, retinal imaging, *in vivo* imaging, animal models, ophthalmology, ophthalmoscopy

**Experimental Biology and Medicine 2021; 246: 2192–2201. DOI: 10.1177/15353702211029582**

## Introduction

Adaptive optics (AO) imaging of the human retina has facilitated extensive investigation of the photoreceptor mosaic over the past 20 years. Beyond describing the distribution of rods and cones within the mosaic,<sup>1–4</sup> the spatial and temporal variability in photoreceptor reflectance has been a topic of great interest. In fact, photoreceptors have been shown to vary in their reflectance over time scales ranging from milliseconds to days.<sup>5–8</sup> The exact mechanism that drives this variability remains unknown, though emerging evidence indicates that the photoreceptors themselves may govern these phenomena.<sup>5,6,8–12</sup> While extant models suggest a variety of origins, it is generally agreed that the unique anatomy of photoreceptors contributes to aspects of light capture, propagation, and reflectance. The role of the photopigment in photoreceptor reflectance has been appreciated since early AO retinal densitometry experiments, where the relative amount of bleached photopigment was shown to correlate with the cone reflectance.<sup>3</sup> More recently, there has been a rapid increase in optophysiological studies characterizing the reflectance and phase-based changes induced by the phototransduction process.<sup>7,10,13–16</sup> Despite these advances, there remain unanswered questions as to how changes in photoreceptor structure, such as those that may occur in disease, affect cone reflectance behavior. For example, while reduced/absent cone reflectance in patients with achromatopsia has been demonstrated by many studies, the anatomical basis of this phenotype is not understood (though the cones are non-functional).<sup>17,18</sup> Conversely, “dysflective cones” have been observed in other conditions—these cones are hyporeflective/non-waveguiding yet retain normal sensitivity.<sup>19–21</sup> Taken together, these data highlight gaps in our understanding of photoreceptor reflectance in AO imagery.

The reliance on human patients presents obstacles to probe the cellular contributions to photoreceptor reflectance changes, as we cannot manipulate the photoreceptors *in vivo* and histological studies are limited. Animal models offer an attractive alternative, given the possibility of genetic and pharmacologic manipulation and *in vivo* versus *ex vivo* comparisons. Mice are a common animal model used for vision research,<sup>22</sup> however, they are not an ideal candidate for investigating cone photoreceptors, as they are rod dominant.<sup>23</sup> The northern tree shrew (*Tupaia belangeri*) and the thirteen-lined ground squirrel (13-LGS, *Ictidomys tridecemlineatus*) are two emerging animal models for vision research.<sup>24,25</sup> They both feature cone-dominant retinas and are amenable to AOSLO and other conventional retinal imaging approaches.<sup>26–28</sup> Additionally, both species have well-documented anatomical differences in their cone photoreceptors compared to humans, which provides an opportunity to test hypotheses about possible shared origins of photoreceptor reflectance behavior. For example, tree shrew cone inner segments contain “megamitochondria”,<sup>29,30</sup> which is relevant as mitochondria have been proposed as a source of contrast in non-confocal split-detection AOSLO.<sup>31</sup> These mitochondria may act as micro-lenses which may help to concentrate

the light within the cones (and could thus affect the waveguiding and reflectance behavior of the cell). Thirteen-lined ground squirrels are obligate hibernators who experience reversible disruptions to their photoreceptor structure during torpor, including narrowing and clumping of cone outer segment discs and a reduced number of inner segment mitochondria.<sup>32</sup> Here we sought to characterize spatial and temporal cone reflectance behavior in these species and compare our findings to those reported in humans.

## Materials and methods

### Animals

Two northern tree shrews (*Tupaia belangeri*, one male and one female) were acquired from the Max Planck Florida Institute for Neuroscience and were housed in accordance with their care and housing recommendations.<sup>33</sup> The northern tree shrews were imaged on 25 November 2019 from 11:30 a.m. to 12:30 p.m. (tree shrew 2) and 1 p.m. to 1:30 p.m. (tree shrew 1). Two captive-born (from a single wild-caught mother) thirteen-lined ground squirrels (*Ictidomys tridecemlineatus*, 13-LGS, one male and one female) were also used in this study. The 13-LGS were weaned and housed as outlined in Merriman *et al.*<sup>34</sup> The 13-LGS used in this study were imaged while in a euthermic state, on 4 March 2020. 13-LGS 1 was imaged from 2:30 p.m. to 3:30 p.m., while 13-LGS 2 was imaged from 9 a.m. to 10:15 a.m. 13-LGS normally undergo hibernation from late October through mid-April; however, the animals used in this study were prevented from hibernating, and were kept in a euthermic state, in a temperature controlled room (68–72°F) with a lighting schedule that was modified every two weeks to match the photoperiod of southern Wisconsin. All experimental procedures performed were approved by the Institutional Animal Care and Use Committee, in an American Association for Accreditation of Laboratory of Animal Care accredited facility.

For imaging, all animals were anesthetized with isoflurane (1–5% for induction and maintenance with a rate of 0.2–1 L/min O<sub>2</sub> for tree shrews, 5% induction and 2–3% maintenance at 1.5 L/min for the 13-LGS) in 1 L/min O<sub>2</sub> using a non-rebreathing system (VetEquip Inc., Livermore, CA, USA). For the tree shrews, a designated anesthesia technician was responsible for monitoring the respirations of the animal and adjusting the concentration of isoflurane accordingly in order to maintain the proper plane of anesthesia needed for imaging. After the proper plane of anesthesia was induced, pupils were dilated and cyclopleged with 2.5% phenylephrine and 1% tropicamide (Akorn, Inc., Lake Forest, IL, USA). Animals were then moved to a heated imaging cassette which was mounted to a positioning stage that allowed translation and rotation of the animal. Anesthesia was maintained with the use of a nose cone, which was attached to the imaging cassette. A pediatric ocular speculum was then placed on the eye that was being imaged. Vaseline® (Unilever US, Inc., Englewood Cliffs, NJ, USA) was used to weigh down any whiskers that were obscuring the pupil.

## AOSLO imaging

Confocal reflectance images were acquired using a previously described custom AOSLO modified for a 4.5 mm system pupil diameter.<sup>28,35</sup> Imaging was performed using a 790 nm superluminescent diode (SLD) along with an 850 nm wavefront sensing source. The optical power measured at the pupil was 355  $\mu$ W for 790 nm and 48  $\mu$ W for 850 nm. Measurement and correction of the wavefront aberrations at the eye were performed using a Shack–Hartmann wavefront sensor and a 7.2 mm diameter 97-actuator ALPAO deformable mirror (ALPAO; Montbonnot-Saint-Martin, France), respectively. A 40- $\mu$ m pinhole ( $\sim$ 1 airy disk diameter) was used in the confocal detection channel.

For each animal, one retinal location (spanning approximately four degrees square of retinal area) was imaged at 5- to 10-min intervals for a total duration of 18–25 min. The retinal location used for imaging was obtained by following a blood vessel from the optic nerve head or optic disk, for reproducibility purposes, then capturing image sequences on either side of the blood vessel. The image sequences, comprised of 100 frames, were captured with a 2° by 2° field of view at a frame rate of 16.67 Hz for a total of  $\sim$ 6 s. The acquisition software allows for automatic rejection of frames below a certain threshold; however, this setting was not used in this study. A maximum of six repeated acquisitions were collected for each animal and some measurements were excluded from analysis due to insufficient overlap or poor image quality. Various eye drops were used to maintain corneal hydration and refresh the natural tear film during imaging: balanced salt solution (BSS), Refresh Plus® (Allergan, Dublin Ireland), Systane® Ultra (Alcon Laboratories Inc., Geneva, Switzerland), and Geri-Care® Artificial Tears (Geri-Care Pharmaceuticals, Brooklyn, New York). Drops were applied between videos as needed and excess fluid wicked away from the lower eyelid using a cellulose surgical spear (DeRoyal, Inc., Powell, TN, USA).

## AOSLO image processing

Image sequences acquired using our AOSLO were subject to distortion due to the sinusoidal motion of the resonant scanner. The distortion was estimated by acquiring images of a Ronchi ruling with 118.1 lines/mm, then corrected by resampling retinal image sequences such that the distortion is removed, and the pixels are equally spaced in both directions. The retinal image sequences were then inspected, and reference frames were manually selected for registration. Strip registration was performed using previously described custom software.<sup>36</sup> The registered and averaged output was inspected, and registration parameters were changed in an iterative manner until all output images were of acceptable quality (no over cropping, registration artifacts, or poor signal-to-noise ratio). By default, the custom registration software used performs min/max contrast stretching on the output images, which could alter the measured reflectance values. To mitigate this, the raw .dat files were exported from the registration software and converted into a non-contrast stretched .tif using the *d1mread*, *uint8*, and *imwrite* functions in MATLAB (MathWorks, Inc.,

Natick, MA, USA); this image was used for subsequent quantitative analyses. A custom python script was then used to mitigate distortion caused by eye movements<sup>37,38</sup> (<https://github.com/OCVL/Eye-Motion-Repair>). This script works by calculating the median ( $x,y$ ) shift for each row across the registered frames in an image sequence then re-warping the sequence to cancel out the median shift (assuming the eye movements are spatially random over time).

At each timepoint, multiple image sequences were acquired near the retinal location of interest in order to maximize the overlap between different time points as seen in panel A of Figure 1. All the registered averaged images were manually inspected and the image from each time point with the most apparent overlap with the images from the other time points was selected for further analysis. Once the best images for each time point were selected, all the images were saved as a .tif stack and .avi using ImageJ.<sup>39</sup> A reference frame that would maximize the amount of overlap between the other time points for each animal was manually selected for registration purposes. For the 13-LGS, the stack of selected images was then loaded into a custom MATLAB (MathWorks, Inc., Natick, MA, USA) scale-invariant feature transform (SIFT) algorithm script for automatic alignment (Figure 1(b)). The alignment results were then manually verified and minor adjustments were performed in Adobe Photoshop (Adobe, Inc. San Jose, CA, USA). The cones in the tree shrew retina have a multimodal appearance, and as such the SIFT algorithm often failed to properly align these images. Therefore, the images for each location in the tree shrews were manually aligned in Adobe Photoshop (Adobe, Inc. San Jose, CA, USA). After the alignment process was complete for both species, the images were cropped to a common area across time, and then saved as an .avi and .tif stack for further analysis (Figure 1(c)).

## Generating reflectance profiles

A composite cone image for each location was created using ImageJ<sup>39</sup> by averaging pixelwise intensity value between the aligned-cropped image stack (ImageJ»Stacks»Z-Project»Average Intensity). A Gaussian blur filter with a standard deviation of two pixels was applied in ImageJ<sup>40</sup> to further aid in identification of the cone coordinates, given the heterogenous reflectance profiles of cones in individual images. This composite image was then input into custom semi-automated cone counting software which provides the coordinates that correspond to the center of each cone (Mosaic Analytics; Translational Imaging Innovations, Hickory, NC, USA). A .csv file of the cone coordinates was saved for subsequent reflectance analysis.

A previously described custom MATLAB (MathWorks, Inc., Natick, MA, USA) script was used to generate the reflectance profiles for each cone.<sup>8</sup> This script takes the .avi containing the aligned time point images and cone coordinate .csv file and uses an eroded Voronoi mask (centered on each cone coordinate) to find the average reflectance for each cone over time. This eroded mask is



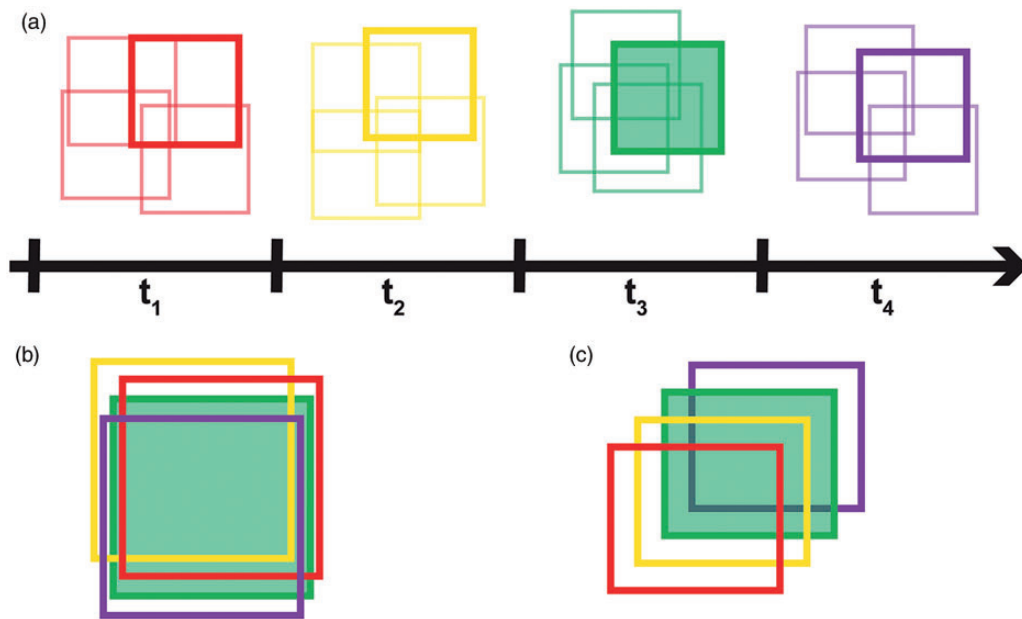


**Figure 1.** Reflectance time series imaging and reference frame selection. (a) Wireframe representation of four time points, where each square represents the processed AOSLO image from each of the four image sequences collected at each time point (see *Methods*). These overlapping image sequences were acquired in order to maximize overlap between time points and compensate for occasional eye drift. The processed image from each time point with the most apparent spatial overlap with the images from the other time points was selected for further analysis (indicated by the bold squares). (b) These images were then aligned to each other either manually (for tree shrews) or by using a SIFT algorithm (for 13-LGS). The green square represents the image used as the reference frame for the SIFT algorithm. (c) The aligned images were then cropped to the common area and saved as a stack in chronological order.

defined by shrinking the original Voronoi mask by two pixels (for the 13-LGS) or five pixels (for the tree shrews) from each edge. Cones with unbounded Voronoi domains (at the edges of the images) were excluded from this analysis. The raw cone reflectance values and a plot of each cone's raw reflectance over time were saved. The reflectance for each cone was also normalized with respect to the mean reflectance value of all the other cones in that time point to account for systematic pixel intensity changes caused by higher signal-to-noise ratio in some images. The raw reflectance values were used for all spatial analyses, while the normalized reflectance values were used for the temporal analyses.

### Analyzing reflectance profiles

In order to analyze the reflectance profiles of each cone spatially and temporally, the cones for each subject were separated into two groups, those with a reflectance profile which varied over time versus those with an invariant reflectance profile. To determine which cones varied over time the coefficient of variation was calculated for each cone. Cones with a coefficient of variation lower than 10% were classified as invariant (8.94% of 13-LGS cones, and 22.5% of tree shrew cones), while all other cones were classified as variable over time. To assess the cell-to-cell spatial reflectance variability, the coefficient of variation was also calculated by assessing all the cones across each individual time point image. To determine if the temporally invariant cones were randomly distributed across the image, we utilized a previously published statistical approach.<sup>41</sup> For each animal, the distances between each cell having an invariant temporal reflectance profile and all of the other cells having

invariant temporal reflectance profiles were calculated. From these data, a cumulative histogram of intercell distances was generated. We then computed the expected minimum, average, and maximum cumulative histogram of intercell distances in 1000 randomly generated mosaics, which each contained the same number of invariant cones as seen in the observed case. The expected cumulative histograms were then compared to the actual cumulative histogram for that particular image. To further distinguish if the invariant cones were randomly distributed throughout the mosaic, we calculated the root mean square deviation (RMSD) between the observed cumulative histogram and the simulated mean cumulative histograms. The RMSD was also calculated between the simulated mean cumulative histogram and each individual simulated mosaic. The distribution of the observed mosaic was indistinguishable from random if the predicted versus observed fraction of cones separation line falling completely within the bounds set by the minimum and maximum cumulative histograms from the 1000 randomly generated mosaics and the RMSD between the observed cumulative histogram and the simulated mean cumulative histograms all fell within the 95th percentile of the RMSD between the mean simulated cumulative histogram and all other simulated cumulative histograms. All statistical analyses were performed using MATLAB (MathWorks, Inc., Natick, MA, USA).

## Results

### Cell-to-cell spatial reflectance variability

We analyzed the reflectance of 2796 cones (525 from the shrews, and 2271 from the 13-LGS) from four animals and

observed clear cell-to-cell reflectance variability in both species (Figure 2). Some cones appear bright (corresponding to a high reflectance), while others appear dim (corresponding to a low reflectance) in comparison. This phenomena can be further observed in the raw reflectance distributions of the analyzed cones for each animal (Figure 3). We present the distributions at the time point which corresponds to the median coefficient of variation of each cone within a single time point for each animal. Note that even at the time points with the minimum coefficient of variation there was still a large amount of cell-to-cell variability in the appearance of individual cones.

### Temporal reflectance variability

Temporal variability in cone photoreceptor reflectance was observed in both species, as has been reported for human cones.<sup>7,10,13–15</sup> Moreover, not all cells change reflectance over time in the same way. Some cells appear to change in a linear or constant manner (either increasing or decreasing), whereas others exhibit oscillatory changes. Other cells remain invariant with no substantial changes in reflectance over time. To quantify the temporal variability, the coefficient of variation for the normalized temporal reflectance values of each cone was calculated. Shown in Figure 4 are individual reflectance traces for three cones in each animal,

representing the cells with the minimum, median, and maximum coefficient of variation. The heterogeneity of the behavior of individual cells for each animal is summarized in Figure 5. The extent of variation across the cones for each animal was similar.

### Distribution of invariant cones

Next, we assessed how the temporal reflectance changes of individual cells were distributed across the image. Shown in Figure 6 are false color overlays of the coefficient of variation over the photoreceptor composite image for each animal. While no obvious pattern was detectable, cumulative histogram comparison plots were used to further determine if the invariant cones were randomly distributed across the image (Figure 7). The arrangement of the invariant cones for all four animals was found to be indistinguishable from random due to the predicted versus observed fraction of cones separation line falling completely within the bounds set by the minimum and maximum cumulative histograms from the 1000 randomly generated mosaics and because the RMSD between the observed cumulative histogram and the simulated mean cumulative histograms all fell within the 95th percentile of the RMSD between the mean simulated cumulative histograms and all other simulated cumulative histograms.

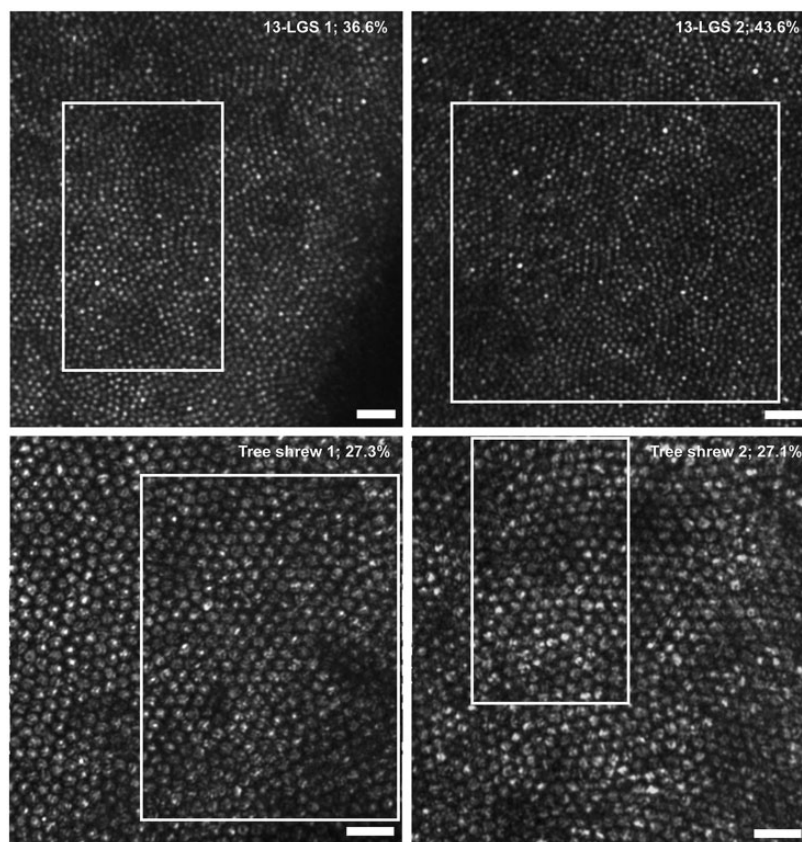


**Figure 2.** Confocal AOSLO images for each animal, highlighting the cell-to-cell variation in cone photoreceptor reflectance at a single time point. The images shown are from the time point which corresponded to the median cell-to-cell coefficient of variation for that animal. Similar cell-to-cell variability in reflectance was seen in the other time points (coefficient of variation ranging from 34.1–39% for 13-LGS 1, 42.1–45.3% for 13-LGS 2, 26.5–34.2% for tree shrew 1, and 25.7–31.6% for tree shrew 2). The white box indicates the common area between other time points that was used for further analysis for that particular animal. Scale bars represent 20  $\mu$ m.

### Discussion

In this study, we demonstrated substantial inter-cone reflectance variability in confocal AOSLO images from both the 13-LGS and northern tree shrew. Such spatial variability of cone reflectance can be seen in previously published AOSLO images from these species,<sup>26</sup> but had not been quantified previously. Additionally, we demonstrated that both species exhibit temporal variability in cone

reflectance and that the temporal reflectance pattern of neighboring cells was indistinguishable from random, as has been reported in the human retina.<sup>8</sup> This suggests at least partial overlap of the physiological mechanisms underlying photoreceptor reflectance across these species.

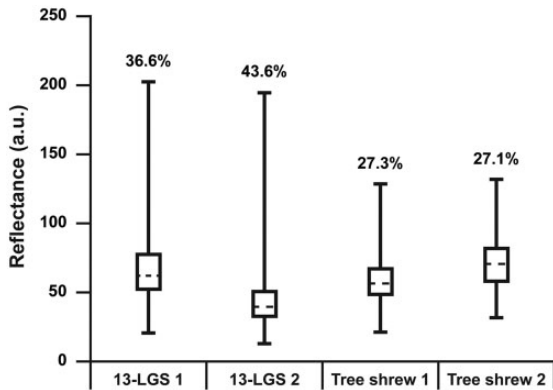


**Figure 3.** Box-and-whisker plots of the distribution of raw cone photoreceptor reflectance for each animal. Shown are data from the individual time points with the median coefficient of variation, as similar variation was shown across all time points for each animal. The corresponding absolute coefficient of variations are indicated above each plot. Shown is the median for each group (horizontal dashed line), while the 25th and 75th percentiles are represented by the lower and upper rectangle boundaries, respectively. Error bars extend to the minimum and maximum values within each group.

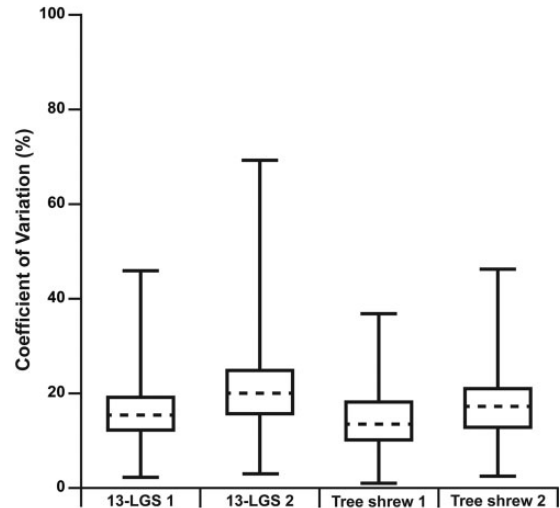


**Figure 5.** Box-and-whisker plots of the coefficient of variation for the temporal reflectance of all analyzed cones for each animal. Shown is the median for each animal (horizontal dashed line), while the 25th and 75th percentiles are represented by the lower and upper rectangle boundaries, respectively. Error bars extend to the minimum and maximum values within each group (individual cones ranged in coefficient of variation from 2.31 to 45.9% for 13-LGS 1, 2.96 to 69.4% for 13-LGS 2, 1.07 to 36.9% for tree shrew 1, and 2.52 to 46.3% for tree shrew 2).

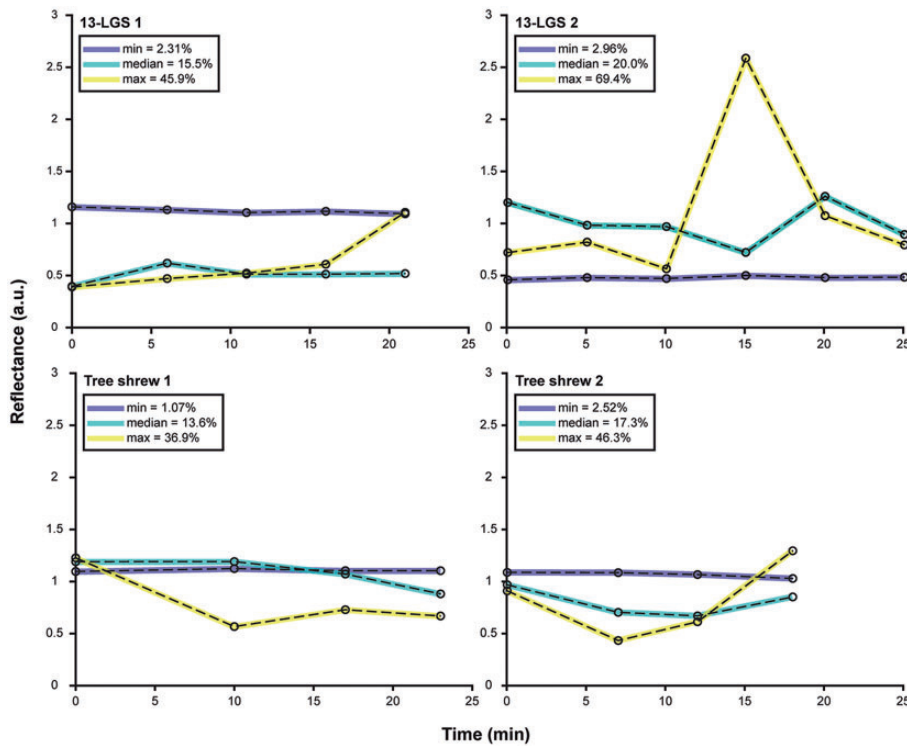


**Figure 4.** Temporal cone reflectance traces for each animal depicting the cone with the minimum (blue), median (cyan), and a maximum (yellow) coefficient of variation across time points. The coefficient of variation expressed in percentage can be seen in the legend in the upper left corner of each plot. Individual cone behavior varied for each animal and variable cone traces showed diverse levels of oscillation and overall slope changes.



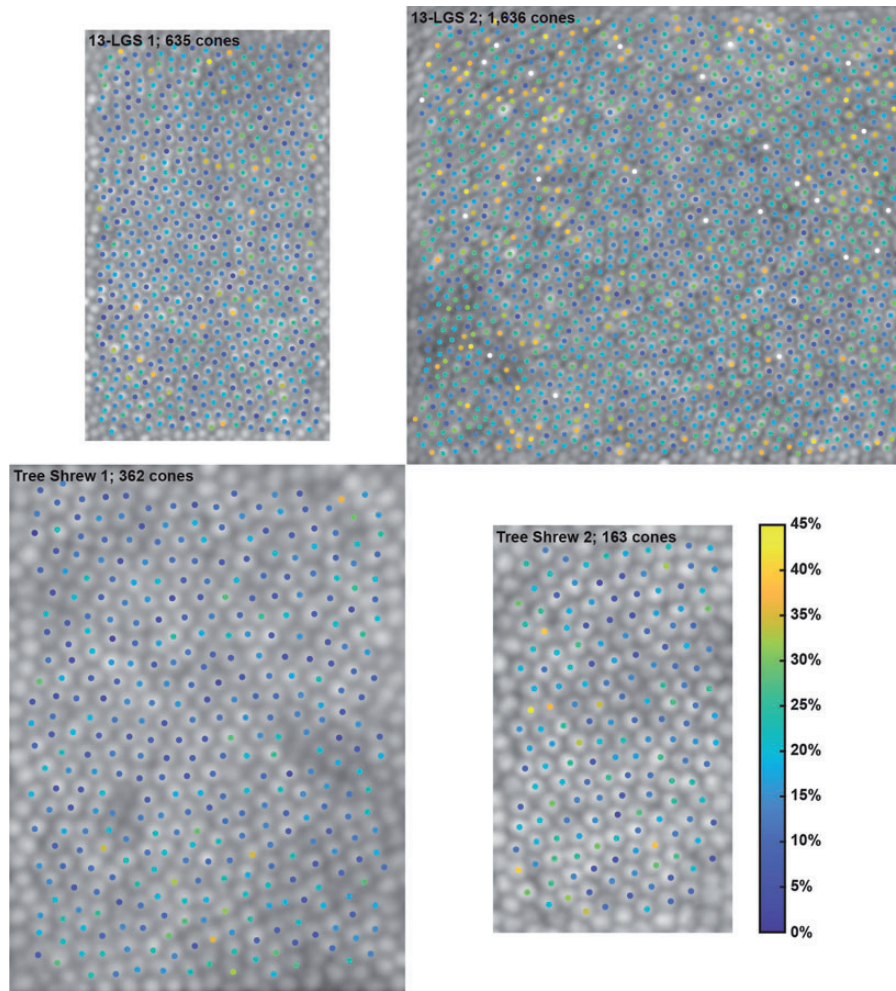


**Figure 6.** False color overlay depicting the coefficient of variation over time for each analyzed cone. Colorbar represents the coefficient of variation expressed in percentage. For visualization purposes, outliers (defined as the 1.5% of cones with the highest coefficient of variation across all animals) are shown in white. The threshold that defines invariant cones can be seen as the white line on the colorbar. No distinct spatial patterns were seen within any animal; however, the cones in 13-LGS 2 had a wider overall range of variation (2.96–69.4%) when compared to the other animals.

Previous studies have suggested that the mitochondria within the cone inner segment act as lenses which help to concentrate light and enhance the coupling between the inner and outer segments of cones.<sup>29</sup> Tree shrew cone inner segments feature large circular megamitochondria in addition to the smaller elongated mitochondria,<sup>30</sup> while the 13-LGS cone inner segments contain tightly packed elongated mitochondria similar to that of humans.<sup>42,43</sup> Our findings suggest that despite the different types and orientation of mitochondria present in the tree shrew, the temporal and spatial reflectance behavior remains similar to that of the 13-LGS (and humans). Mitochondria have also been proposed as a source of contrast in non-confocal split-detection AOSLO (which provides a method to visualize the cone inner segments independent of the waveguided reflection from the outer segment),<sup>31</sup> as well as a source of reflectance on optical coherence tomography (OCT) imaging.<sup>44,45</sup> Future studies may look to alter cone mitochondria structure in these animal models and explore changes in confocal and split-detection AOSLO as well as OCT.

There were a number of limitations in this study. First, our current anesthesia protocol limits the total duration and possible time intervals in which AOSLO images can be acquired. It is also challenging to maintain the proper plane of anesthesia needed for imaging in the tree shrews using our current protocol which can lead to issues with eye drift (leading to challenges finding the same retinal location from previous time points). Thus, there is a need to explore alternative anesthesia protocols in these species which will allow future studies to investigate this behavior over a longer time period (hours, days, etc.). Secondly, the coarse sampling between time points could lead to temporal reflectance aliasing, to mitigate this future studies should investigate the temporal reflectance behavior at closer time intervals. Additionally, results were based on a total of only four eyes. While there is no reason to expect that these results would be qualitatively different for other eyes, there could be quantitative differences due to factors like age or sex that will require larger studies to elucidate. Finally, the analysis methods are somewhat time consuming and have multiple manual steps, more routine

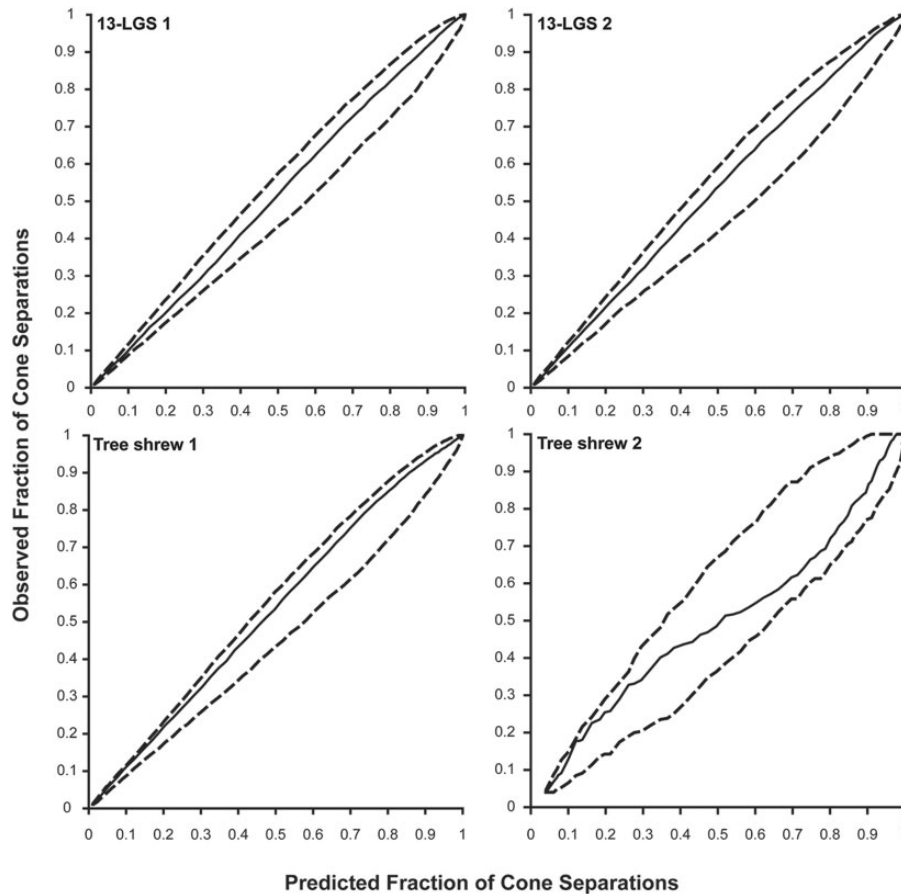


**Figure 7.** Cumulative histogram comparison for invariant cones. The solid line represents the average predicted fraction of cone separations from 1000 randomly simulated cone mosaics versus the observed fraction of the inter-cell distances. The dashed lines represent the minimum and maximum bounds of the predicted fraction of cone separations from the random simulations. The distribution of invariant cones was determined to be indistinguishable from random for each animal in this study, as the solid line does not fall outside of the minimum and maximum bounds set by the dashed lines and the root mean square deviation (RMSD) of the observed and predicted fraction of cone separations did not fall outside of the 95th percentile from the RMSD of the predicted cone separations and the mean predicted cone separations.

assessment of cone reflectance will require further automation of the analysis pipeline. Advances in automated processing of AOSLO imaging,<sup>46</sup> combined with automated algorithms for cone identification and segmentation,<sup>47–49</sup> should be beneficial in these efforts.

The cones in the 13-LGS undergo significant anatomical changes during torpor, such as narrowing and clumping of cone outer segment disks and the reduction of inner segment mitochondria.<sup>32</sup> While this results in an overall decrease in AOSLO image quality,<sup>32</sup> it is not clear whether cones exhibit similar temporal reflectance variability during torpor. As these changes are naturally reversible,<sup>32</sup> comparing the behavior of individual cones during different phases of the hibernation cycle could provide important insight into the anatomical factors underlying cone reflectivity on AOSLO imagery. The cones in both species exhibit human-like cone reflectance behavior which motivates application of more advanced methods that directly probe cone function.<sup>10,16</sup> This is especially powerful as one could use pharmacological approaches to alter specific aspects of cone structure or function. Thus, these species serve as valuable models on which to test specific hypotheses about stimulus-evoked cone reflectance changes.

Beyond informing models of cone photoreceptor reflectance, such studies will serve to advance both species as models for vision research.

#### AUTHORS' CONTRIBUTIONS

All authors participated in the review of the manuscript, MG, RFC, HMF, AES, and JC participated in the design, analysis, and interpretation of results from this study, MG, JAC, HMF, and CTY conducted the experiment, SF and DKM provided the animals used in this study as well as their general expertise on the care and husbandry of these species, and MG and JC wrote the manuscript.

#### ACKNOWLEDGMENTS

The authors would like to thank Christine Skumatz, Kenneth Allen, Lisa King and the Biomedical Resource Center at the Medical College of Wisconsin for their help with tree shrew and 13-LGS care, Alfredo Dubra for developing the AOSLO and supporting software, Brian Higgins for data management and storage support, and David Fitzpatrick for input on tree shrew logistics.






## DECLARATION OF CONFLICTING INTERESTS

RFC has financial interest and serves as a consultant for Translational Imaging Innovations, AES is currently employed by Translational Imaging Innovations, and JC has financial interest in Translational Imaging Innovations, and receives research funding from Applied Genetic Technologies Corporation, Optovue, and MeiraGTx. All remaining authors report no conflicting financial relationships.

## FUNDING

This work was supported in part by the National Eye Institute of the National Institutes of Health (NIH) under award numbers U24EY029891 and T32EY014537 and by the National Center for Advancing Translational Sciences of the NIH under award number UL1TR001436. This investigation was conducted in a facility constructed with the support from the Research Facilities Improvement Program, grant number C06RR016511 from the National Center for Research Resources, NIH. The content of this publication is solely the responsibility of the authors and does not necessarily represent the official views of the NIH. Additional support was provided by the Foundation Fighting Blindness grant number FFB PPA-0641-0718-UCSF and the ALCON Research Institute.

## ORCID iDs

Mina Gaffney  <https://orcid.org/0000-0001-5076-3354>  
 Jenna A Cava  <https://orcid.org/0000-0002-9128-6897>  
 Dana K Merriman  <https://orcid.org/0000-0003-2780-0772>

## REFERENCES

- Cooper RF, Wilk MA, Tarima S, Carroll J. Evaluating descriptive metrics of the human cone mosaic. *Invest Ophthalmol Vis Sci* 2016;**57**:2992–3001
- Doble N, Choi SS, Codana JL, Christou J, Enoch JM, Williams DR. In vivo imaging of the human rod photoreceptor mosaic. *Opt Lett* 2011;**36**:31–3
- Roorda A, Metha AB, Lennie P, Williams DR. Packing arrangement of the three cone classes in primate retina. *Vision Res* 2001;**41**:1291–306
- Duncan JL, Zhang Y, Gandhi J, Nakanishi C, Othman M, Branham KE, Swaroop A, Roorda A. High-resolution imaging with adaptive optics patients with inherited retinal degeneration. *Invest Ophthalmol Vis Sci* 2007;**48**:3283–91
- Pircher M, Kroisamer JS, Felberer F, Sattmann H, Götzinger E, Hitznerberger CK. Temporal changes of human cone photoreceptors observed in vivo with SLO/OCT. *Biomed Opt Express* 2010;**2**:100–12
- Pallikaris A, Williams DR, Hofer H. The reflectance of single cones in the living human eye. *Invest Ophthalmol Vis Sci* 2003;**44**:4580–92
- Jonnal RS, Besecker JR, Derby JC, Kocaoglu OP, Cense B, Gao W, Wang Q, Miller DT. Imaging outer segment renewal in living human cone photoreceptors. *Opt Express* 2010;**18**:5257–70
- Cooper RF, Dubis AM, Pavaskar A, Rha J, Dubra A, Carroll J. Spatial and temporal variation of rod photoreceptor reflectance in the human retina. *Biomed Opt Express* 2011;**2**:2577–89
- Jonnal RS, Rha J, Zhang Y, Cense B, Gao W, Miller DT. In vivo functional imaging of human cone photoreceptors. *Opt Express* 2007;**14**:16141–60
- Cooper RF, Tuten WS, Dubra A, Brainard DH, Morgan JIW. Non-invasive assessment of human cone photoreceptor function. *Biomed Opt Express* 2017;**8**:5098–112
- Meadway A, Sincich LC. Light propagation and capture in cone photoreceptors. *Biomed Opt Express* 2018;**9**:5543–65
- Vohnsen B. Directional sensitivity of the retina: a layered scattering model of outer-segment photoreceptor pigments. *Biomed Opt Express* 2014;**5**:1569–87
- Zhang P, Zawadzki RJ, Goswami M, Nguyen PT, Yarov-Yarovoy Y, Burns ME, Pugh EN. Jr. In vivo optophysiology reveals that G-protein activation triggers osmotic swelling and increased light scattering of rod photoreceptors. *Proc Natl Acad Sci U S A* 2017;**114**:E2937–E46
- Sabesan R, Hofer H, Roorda A. Characterizing the human cone photoreceptor mosaic via dynamic photopigment densitometry. *PLoS One* 2015;**10**:e0144891
- Cooper RF, Brainard DH, Morgan JIW. Optoretinography of individual human cone photoreceptors. *Opt Express* 2020;**28**:39326–39
- Pandiyan VP, Maloney-Bertelli A, Kuchenbecker JA, Boyle KC, Ling T, Chen ZC, Park BH, Roorda A, Palanker D, Sabesan R. The optoretinogram reveals the primary steps of phototransduction in the living human eye. *Sci Adv* 2020;**6**:eabc1124
- Langlo CS, Patterson EJ, Higgins BP, Summerfelt P, Razeen MM, Erker LR, Parker M, Collison FT, Fishman GA, Kay CN, Zhang J, Weleber RG, Yang P, Wilson DJ, Pennesi ME, Lam BL, Chiang J, Chulay JD, Dubra A, Hauswirth WW, Carroll J. ACHM-001 study group. Residual foveal cone structure in CNGB3-associated achromatopsia. *Invest Ophthalmol Vis Sci* 2016;**57**:3984–95
- Genead MA, Fishman GA, Rha J, Dubis AM, Bonci DM, Dubra A, Stone EM, Neitz M, Carroll J. Photoreceptor structure and function in patients with congenital achromatopsia. *Invest Ophthalmol Vis Sci* 2011;**52**:7298–308
- Tu JH, Foote KG, Lujan BJ, Ratnam K, Qin J, Gorin MB, Cunningham ET, Jr., Tuten WS, Duncan JL, Roorda A. Dysflective cones: visual function and cone reflectivity in long-term follow-up of acute bilateral foveolitis. *Am J Ophthalmol Case Rep* 2017;**7**:14–9
- Duncan JL, Roorda A. Dysflective cones. *Adv Exp Med Biol* 2019;**1185**:133–7
- Bruce KS, Harmening WM, Langston BR, Tuten WS, Roorda A, Sincich LC. Normal perceptual sensitivity arising from weakly reflective cone photoreceptors. *Invest Ophthalmol Vis Sci* 2015;**56**:44313–8
- Slijkerman RW, Song F, Astuti GD, Huynen MA, van Wijk E, Stieger K, Collin RW. The pros and cons of vertebrate animal models for functional and therapeutic research on inherited retinal dystrophies. *Prog Retin Eye Res* 2015;**48**:137–59
- Carter-Dawson LDL, MM. Rods and cones in the mouse retina. I. Structural analysis using light and electron microscopy. *J Comp Neurol* 1979;**188**:245–62
- Cao J, Yang EB, Su JJ, Li Y, Chow P. The tree shrews: adjuncts and alternatives to primates as models for biomedical research. *J Med Primatol* 2003;**32**:123–30
- Van Hooser SD, Nelson SB. The squirrel as a rodent model of the human visual system. *Vis Neurosci* 2006;**23**:765–78
- Sajdak BS, Salmon AE, Cava JA, Allen KP, Freling S, Ramamirtham R, Norton TT, Roorda A, Carroll J. Noninvasive imaging of the tree shrew eye: wavefront analysis and retinal imaging with correlative histology. *Exp Eye Res* 2019;**185**:107683
- Sajdak BS, Salmon AE, Linderman RE, Cava JA, Heitkotter H, Carroll J. Interocular symmetry, intraobserver repeatability, and interobserver reliability of cone density measurements in the 13-lined ground squirrel. *PLoS One* 2019;**14**:e0223110
- Sajdak BS, Sulai YN, Langlo CS, Luna G, Fisher SK, Merriman DK, Dubra A. Noninvasive imaging of the thirteen-lined ground squirrel photoreceptor mosaic. *Vis Neurosci* 2016;**33**:e003
- Knabe W, Skatchkov S, Kuhn HJ. "Lens mitochondria" in the retinal cones of the tree-shrew tupaia belangeri. *Vision Res* 1997;**37**:267–71
- Samorajski T, Ordy JM, Keefe JR. Structural organization of the retina in the tree shrew (*tupaia glis*). *J Cell Biol* 1966;**28**:489–504
- Scoles D, Sulai YN, Langlo CS, Fishman GA, Curcio CA, Carroll J, Dubra A. In vivo imaging of human cone photoreceptor inner segments. *Invest Ophthalmol Vis Sci* 2014;**55**:4244–51
- Sajdak BS, Bell BA, Lewis TR, Luna G, Cornwell GS, Fisher SK, Merriman DK, Carroll J. Assessment of outer retinal remodeling in the hibernating 13-lined ground squirrel. *Invest Ophthalmol Vis Sci* 2018;**59**:2538–47

33. Freling S. *Learning about tree shrews*. Memphis, TN: American Association for Laboratory Animal Science, 2018, pp.14–17.
34. Merriman DK, Lahvis G, Jooss M, Gesicki JA, Schill K. Current practices in a captive breeding colony of 13-lined ground squirrels (*ictidomys tridecemlineatus*). *Lab Anim* 2012;**41**:315–25
35. Dubra A, Sulai Y. Reflective afocal broadband adaptive optics scanning ophthalmoscope. *Biomed Opt Express* 2011;**2**:1757–68
36. Dubra A, Harvey Z. Registration of 2D images from fast scanning ophthalmic instruments. In: Fischer B, Dawant B, Lorenz C (eds) *Biomedical image registration*. 1st. ed. Berlin: Springer-Verlag, 2010, pp. 60–71
37. Chen M, Cooper RF, Gee JC, Brainard DH, Morgan JIW. Automatic longitudinal montaging of adaptive optics retinal images using constellation matching. *Biomed Opt Express* 2019;**10**:6476–96
38. Bedgood P, Metha A. De-warping of images and improved eye tracking for the scanning laser ophthalmoscope. *PLoS One* 2017;**12**:e0174617
39. Schneider CA, Rasband WS, Eliceiri KW. NIH image to ImageJ: 25 years of image analysis. *Nat Methods* 2012;**9**:671–5
40. Schneider E, Zimmermann H, Oberwahrenbrock T, Kaufhold F, Kadas EM, Petzold A, Bilger F, Borisow N, Jarius S, Wildemann B, Ruprecht K, Brandt AU, Paul F. Optical coherence tomography reveals distinct patterns of retinal damage in neuromyelitis optica and multiple sclerosis. *PLoS One* 2013;**8**:e66151
41. Diggle PJ. Statistical analysis of spatial point patterns. In: Sibson R, Cohen JE (eds) *Mathematics in biology*. London: Academic Press, 1983
42. West RW, Dowling JE. Anatomical evidence for cone and rod-like receptors in the gray squirrel, ground squirrel, and prairie dog retinas. *J Comp Neurol* 1975;**159**:439–60
43. Sajdak BS, Salmon AE, Litts KM, Wells C, Allen KP, Dubra A, Merriman DK, Carroll J. Evaluating seasonal changes of cone photoreceptor structure in the 13-lined ground squirrel. *Vision Res* 2019;**158**:90–9
44. Litts KM, Zhang Y, Freund KB, Curcio CA. Optical coherence tomography and histology of age-related macular degeneration support mitochondria as reflectivity sources. *Retina* 2018;**38**:445–61
45. Wilson JD, Cottrell WJ, Foster TH. Index-of-refraction-dependent sub-cellular light scattering observed with organelle-specific dyes. *J Biomed Opt* 2007;**12**:014010
46. Salmon AE, Cooper RF, Langlo CS, Baghaie A, Dubra A, Carroll J. An automated reference frame selection (ARFS) algorithm for cone imaging with adaptive optics scanning light ophthalmoscopy. *Transl Vis Sci Technol* 2017;**6**:9
47. Davidson B, Kalitzeos A, Carroll J, Dubra A, Ourselin S, Michaelides M, Bergeles C. Automatic cone photoreceptor localisation in healthy and stargardt afflicted retinas using deep learning. *Sci Rep* 2018;**8**:7911
48. Cunefare D, Cooper RF, Higgins B, Katz DF, Dubra A, Carroll J, Farsiu S. Automatic detection of cone photoreceptors in split detector adaptive optics scanning light ophthalmoscope images. *Biomed Opt Express* 2016;**7**:2036–50
49. Cunefare D, Fang L, Cooper RF, Dubra A, Carroll J, Farsiu S. Open source software for automatic detection of cone photoreceptors in adaptive optics ophthalmoscopy using convolutional neural networks. *Sci Rep* 2017;**7**:6620

(Received March 31, 2021, Accepted June 14, 2021)